Chemical Engineering Journal 445 (2022) 136790

Contents lists available at ScienceDirect

Chemical Engineering Journal

journal homepage: www.elsevier.com/locate/cej

Self-assembled sulphur doped carbon nitride for photocatalytic water reforming of methanol

Hui Wang [a], Madasamy Thangamuthu [a], Zhibin Wu [b], Jianlong Yang [c], Hongzhao Yuan [d], Junwang Tang [a,*]

[a] Department of Chemical Engineering, University College London, London WC1E 7JE, UK
[b] College of Resources and Environment, Hunan Agricultural University, Changsha 410128, PR China
[c] Key Lab of Synthetic and Natural Functional Molecule Chemistry of Ministry of Education, the Energy and Catalysis Hub, College of Chemistry and Materials Science, Northwest University, Xi'an 710127, PR China
[d] Key Laboratory of Agro-ecological Processes in Subtropical Region, Institute of Subtropical Agriculture, Chinese Academy of Sciences, Mapoling, Changsha, Hunan, 410125, PR China

ARTICLE INFO

Keywords:
Doped graphitic carbon nitride
C-S-H bonds
Water reforming of methanol
Photocatalysis
High stability
H_2 production

ABSTRACT

The ability to effectively harness and store renewable solar energy in chemical forms, e.g., methanol has been widely recognised as a promising and sustainable strategy for H_2 storage. Though traditional steam reforming of methanol enables effective H_2 release from methanol and water, the harsh operating conditions result in high energy consumption and CO by-product. To minimize CO emission and maximise H_2 production, photocatalytic liquid water reforming of methanol has been developed to produce H_2 by sulphur doped graphitic carbon nitride (SCN) in this work. Consequently, both H_2 and carbon dioxide (CO_2) can be evolved in an ideal ratio of 3:1 and H_2 yield has been found to be dependent on pH and the reaction temperature. A stable and reproducible H_2 evolution rate of 14.7 mmol $g^{-1}h^{-1}$ from water/methanol over 95 h without CO evolution has been achieved, with an apparent quantum efficiency (AQE) of *c.a.* 30 % at 365 nm. The sulphur was found to exist as N-S-H and C-S-H bonds in the SCN photocatalysts, while the latter was found to be well correlated to the photocatalytic activity of H_2 production. Such sulfur doping narrows the bandgap and offers enhanced charge separation, thus leading to enhanced photocatalytic activity.

1. Introduction

H_2 is regarded as the key vector for a zero-carbon economy while it is very challenging for direct H_2 storage and transport. The high hydrogen content (12.6 wt%), easy transportation and storage of methanol promise it to be a favourable liquid H_2 storage medium. Thus traditional H_2 generation by steam reforming of methanol has been investigated extensively, but its operation temperature (200 °C – 350 °C) is much higher than that of fuel cells and results in CO by-product. Moreover, CO as a critical assessment of a hydrogen production technology might affect H_2 use. Thus, developing a low temperature process for H_2 release from methanol without CO by-product is imperative.

Recently, water reforming of methanol has been proposed, where extracting H_2 from water/methanol mixture is more attractive than the steam reforming of methanol with high by-product CO [1]. In this way, not only the hydrogen stored in methanol can be released, but also equimolar water can be activated for additional H_2 production, thus producing more H_2 and also eliminating CO emission. Several catalysts have been developed to realize efficient water reforming of methanol at relatively low temperatures to minimize CO emission [2–4], suggesting the crucial role of water in the methanol conversion. Recently, atomic Pt/α-MoC was reported to realize efficient aqueous methanol-reforming, thus reaching relatively low-temperature H_2 generation from methanol and water. Despite the outstanding efficiency, the operation temperature (>190 °C) still requires extra energy input. One potential strategy for producing clean and renewable H_2 fuel is through photocatalysis [5]. Hence, low-temperature solar-driven water reforming of methanol is highly desirable for minimizing CO generation and cutting the energy cost.

Polymeric carbon nitride (g-C_3N_4) is of great interest due to its attractive properties including the special 2-D structure, easy functionalization and excellent stability [6]. g-C_3N_4 is limited for utilizing the UV

* Corresponding author.
E-mail address: junwang.tang@ucl.ac.uk (J. Tang).

https://doi.org/10.1016/j.cej.2022.136790

Available online 6 May 2022

and little visible light due to the wide bandgap of ca. 2.7 eV and rapid charge recombination, resulting in low photocatalytic efficiency [7,8]. Extensive efforts have been made to alter the g-C_3N_4 structure to harvest a greater proportion of visible photons and to improve charge separation while keeping its negative conduction band for H_2 production [9]. The polymerization pathway has reportedly affected the structure and then its catalytic activity [10,11]. Several strategies have been explored to promote the photocatalytic activity of g-C_3N_4, including heterojunction, cocatalysts modification, surface engineering and so on [12–16]. Among them, elemental doping seems to be the cost-efficient technology to modulate the electronic structure of g-C_3N_4 and thus enhance the activity [17,18]. Though doping a small amount of sulphur (<1.0 wt%) was indicated to promote the photocatalytic efficiency of g-C_3N_4 for hydrogen generation [19,20], in most cases the sulphur was doped in the tri-heptazine or linkages that reduced the crystallinity of g-C_3N_4, leading to moderate activity improvement. The various sulphur doping positions might trigger the different effects on the final physical/chemical properties of g-C_3N_4. The distribution of linkers in heptazine units was also reported to change the band structure of polymers, which could be manipulated during the polymerization [21]. Hence, controlling sulphur doping position is still challenging while it could improve the photocatalytic activity of g-C_3N_4. In addition, few studies focus on the water reforming of methanol using polymer photocatalysts.

Recently, our group has discovered novel strategies to promote the efficiency of polymer photocatalysts by rationally controlling the position of the linker and tuning the polymerization degree of the precursors [6,22], by which the band structure of polymers could be successfully adjusted for photocatalysis. Inspired by oxygen doped g-C_3N_4 derived from semicarbazide hydrochloride [22], thiosemicarbazide was selected as a sulphur-containing precursor to directly synthesise sulphur doped g-C_3N_4 (SCN). The prepared SCN exhibited around 2.5 times higher photocatalytic activity for water reforming of methanol compared to the reference dicyandiamide-derived g-C_3N_4 under visible light irradiation. The reaction conditions, such as temperature, CH_3OH to water ratio, and pH were optimized to further improve the H_2 generation efficiency up to 14.7 mmol $g^{-1}h^{-1}$. In addition, this S-doped polymer photocatalyst exhibited reproducible and stable activity up to 95 h suggesting its excellent stability. A series of characterizations were carried out to investigate the photocatalytic mechanism. The results showed that the rapid charge separation could be obtained after the sulphur introduction and the formed C-S-H groups dominate the activity.

2. Material and methods

2.1. Synthesis

10 g thiosemicarbazide was put in the crucible followed by 4 h of calcination at 500 °C, 550 °C, and 600 °C to obtain sulphur doped C_3N_4 powder (denoted SCN 500, SCN 550, SCN 600), which were then washed by water for three times and separated using a centrifuge (9000 rpm for 5 min). The reference g-C_3N_4 was obtained using the Dicyandiamide as the precursor by 4 h calcination at 550 °C.

2.2. Characterization

The powder X-ray diffraction (XRD) was carried out using Bruker D4 diffractometer equipped with Cu-K*α* source (Kα1 = 1.540562 Å and Kα2 = 1.544398 Å). Ultraviolet–visible diffuse reflectance spectra (UV–vis DRS) were acquired by a Shimadzu UV–Vis 2550 spectrophotometer fitted with an integrating sphere, using standard barium sulfate as a reference. The morphology and microstructure were investigated by the scanning electron microscope (SEM) (Sirion 200). The transmission electron microscopy (TEM) images were collected using a JEOL 2010 instrument. Electron spin resonance (EPR) spectra were collected from Agilent 4100 microwave plasma-atomic emission spectrometer. Photoluminescence (PL) spectra were obtained by Renishaw InVia Raman using 325 nm as the excitation wavelength. XPS data were recorded from a Kratos Axis SUPRA XPS fitted with a monochromatic Al kα X-ray source (1486.7 eV), a spherical sector analyser and three multichannel resistive plates, 128 channel delay line detectors. Data were analysed using Avantage software and the spectra were calibrated with C1s peak at 284.8 eV. The nitrogen adsorption–desorption isotherms were obtained by a Tristar II 3020 analyzer (Micromeritics, USA). The H isotope experiment was performed using 50% deuterated methanol aqueous solution. The gas after the reaction was injected in MAT253 isotope ratio mass spectrometer (Thermo-Fisher Scientific, Walthan, MA, USA) coupled with GasBench-II Interface and sample preparation device including a GC PAL autosampler for product analysis.

2.3. Photocatalytic test

The photocatalytic activity of the samples for water reforming of methanol toward H_2 generation was observed in a 185 mL reactor under a 300 W Xe lamp. Typically, 5 mg of the photocatalyst and a known concentration of H_2PtCl_4 were dispersed in 40 mL aqueous methanol solution (0% − 100%). The suspension was sonicated for 5 min followed by the argon purging to remove oxygen. During the reaction, the gas was withdrawn at a certain time to analyse the produced gases using GC. Apart from the experiment for Pt amount optimisation, other experiments were carried out using 1% Pt as the cocatalyst.

2.4. Apparent quantum efficiency (AQE) measurement

The AQE calculation follows the below equation [23].

$$\mathrm{AQE} = \frac{2 \times \text{the number of generated } H_2 \text{ molecules}}{\text{the number of incident photons}} \times 100\%$$

The measurements were carried out under 365 nm LED irradiation (Perfect Light, Beijing)) and the irradiated diameter was 4 cm.

2.5. Photoelectrochemical test

The PEC tests were carried out using a three-electrode photoelectrochemical cell, where the FTO electrode coated with the photocatalyst was used as the working electrode, and the platinum plate acted as the counter electrode, and the Ag/AgCl electrode acted as the reference electrode. Sunlight simulated with a 150 W xenon lamp (Newport) equipped with an AM 1.5 filter was used as the light source and 0.5 M K_2SO_4 solution was used as the electrolyte. The electrochemical impedance spectra were acquired using the same three-electrode system with the following parameters: at 1.35 V vs. Ag/AgCl and amplitude 0.05 V. The obtained potentials vs. Ag/AgCl were converted to RHE using the Nernst equation $V_{RHE} = V_{Ag/AgCl} + 0.059\,pH + 0.1976$.

3. Results and discussion

3.1. Structure and morphology

A series of characterizations were conducted to investigate the structure and morphology of the prepared photocatalysts. The crystal structures of samples were examined by XRD (Fig. 1a), all samples exhibit similar XRD patterns with two strong diffraction peaks located at 27.4° (0 0 2) and 12.8° (1 0 0), assigned to the structural packing of tri-s-triazine heterocycles and in-plane periodic repeat units of heptazine, respectively [24]. Compared to the reference g-C_3N_4, SCN samples show broader peaks with reduced intensities, probably ascribing to vacancy introduction or reduced layered spacing [25]. Moreover, higher angle shifts are observed in SCN samples, probably attributing to the reduced layer spacing in SCN samples [26]. In addition, the crystallinity of the SCN samples becomes stronger while increasing the calcination temperature from SCN 500 to SCN 550 and SCN 600, which might affect the photocatalytic activity [27]. The full width at half maximum (FWHM)

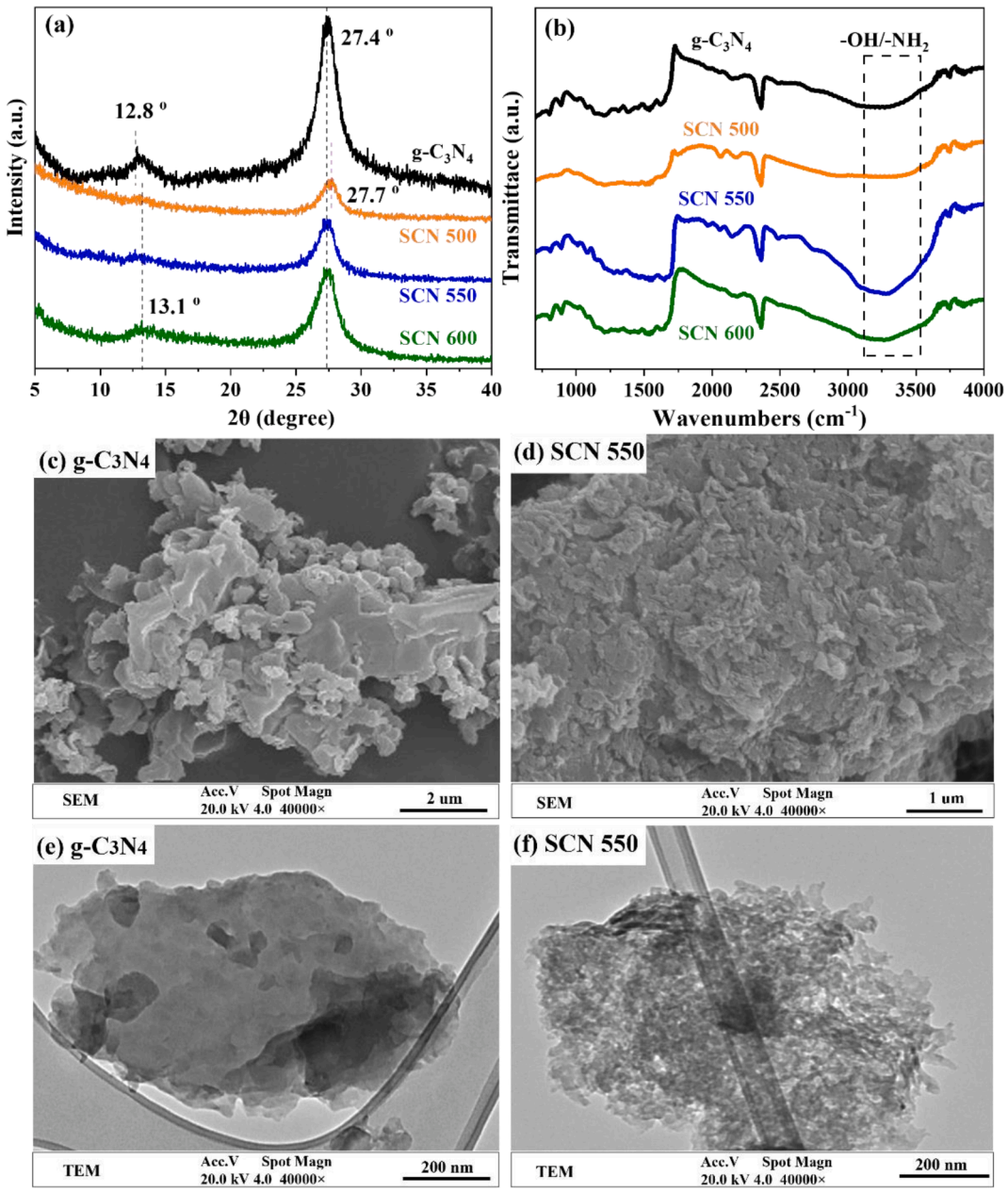

Fig. 1. (a) XRD and (b) FTIR of the reference g-C_3N_4 and SCN samples obtained at various calcination temperatures. The SEM and TEM of (c, e) reference g-C_3N_4 and (d, f) SCN 550.

follows SCN 500 (1.63) < SCN 550 (1.85) < SCN 600 (2.15), suggesting that SCN 600 has the smallest crystal size. Hence, sulphur doping during self-polymerization significantly affects the patterns and topology.

The chemical structures of SCN samples and the reference g-C_3N_4 were closely studied by Fourier transform infrared (FTIR) spectroscopy, and the results are illustrated in Fig. 1b. The typical peaks attributed to carbon nitride have remained in these samples. In particular, the region from 3000 to 3500 cm^{-1} corresponds to the stretching of N–H or O–H motifs in samples originating from surface NH/NH_2 groups and adsorbed H_2O molecules [28]. In detail, the SCN 500 exhibits reduced intensity in this range, indicating that fewer $–NH/NH_2$ groups are present in SCN 500 compared to bare g-C_3N_4. This phenomenon might be ascribed to the N-S-H or -S-H formation instead of the $–NH/NH_2$ group after sulphur introduction. While SCN 550 exhibits a stronger signal, probably due to the more formed $–NH_2$ caused by sulphur evaporation. For SCN 600, there is a similar intensity from 3000 to 3500 cm^{-1} to g-C_3N_4, which might be attributed to both reduced sulphur and NH_2 compared with SCN 550.

The SEM was used to study the morphology of g-C_3N_4 and SCN. g-C_3N_4 presents bulk and smooth particles (Fig. 1c), matching with the reported [29]. In contrast, an inevitable heterogeneity and surface roughness can be seen for the SCN 550 structure (Fig. 1d), probably attributed to the folded structure. Further, the TEM investigation shows the nanosheet's morphology in both samples. The smooth and condensed sheets are observed in g-C_3N_4 (Fig. 1e) while the curly sheets with pore structure exist in SCN 550 (Fig. 1f), which might be due to the effect of sulphur during the polymerization.

3.2. Photocatalytic activity

The H_2 generation activity of g-C_3N_4 and SCN 550 was investigated. As shown in Fig. 2a, SCN 550 exhibits 7 times higher H_2 evolution activity (400 μmol $g^{-1}h^{-1}$) than the typical g-C_3N_4 (58 μmol $g^{-1}h^{-1}$) under visible irradiation ($\lambda > 420$ nm). It also shows 2.5 times higher activity

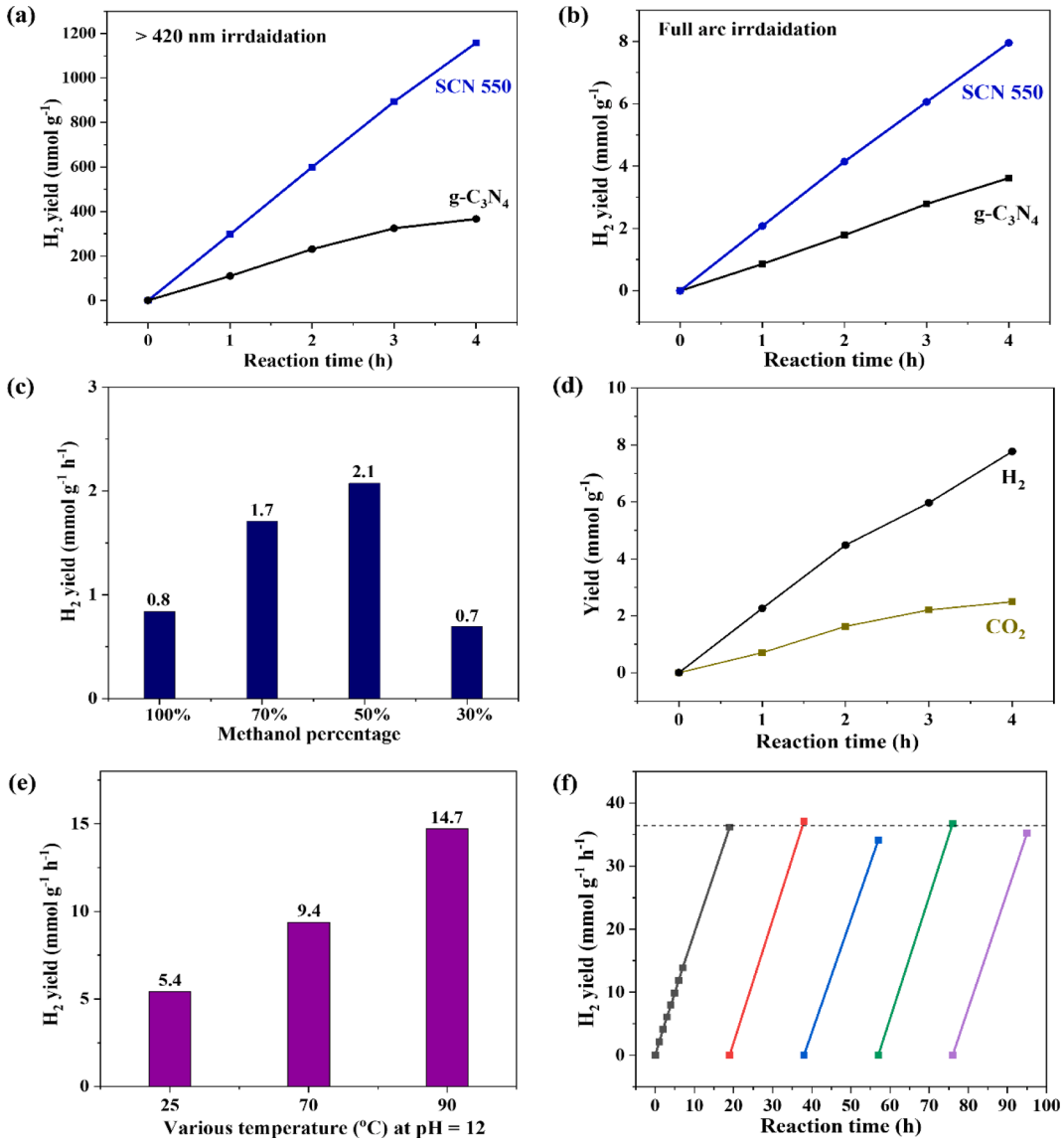

Fig. 2. The activity for H_2 production from water reforming of methanol on g-C_3N_4 and SCN 550 under (a) visible light and (b) full arc irradiation. (c) The photocatalytic H_2 generation activity of SCN (550 °C for 4 h) with the different ratios of methanol to water. (d) The CO_2 and H_2 production on SCN 550 under full arc irradiation. (e) The photocatalytic H_2 generation activity of SCN 550 at various temperatures and pH = 12. (f) The long-term H_2 generation activity of SCN 550 under full arc irradiation.

compared with typical g-C_3N_4 under full arc irradiation (Fig. 2b). All these indicate that sulphur doping increases the liquid water reforming of methanol. Further optimisation studies were undertaken. g-C_3N_4 synthesis conditions might affect the crystallinity of the samples as observed in Fig. 1a and thus delivering various photocatalytic activities. The SCN samples synthesized at different annealing temperatures (500 °C – 600 °C) were studied for water reforming of methanol. While increasing the calcination temperature from 500 °C to 550 °C (Fig. S1), the increased H_2 generation activity is observed from 1.3 mmol $g^{-1}h^{-1}$ to 2.1 mmol $g^{-1}h^{-1}$. It might be due to the better crystallinity obtained at 550 °C compared to 500 °C, as proved by the XRD result (Fig. 1a). Further increasing the calcination temperature to 600 °C leads to a reduced activity (1.6 mmol $g^{-1}h^{-1}$), which might be due to the sulphur removal at high temperature or doping position difference, which will be investigated by XPS.

Then, the impact of different Pt contents on photocatalytic performance was studied and optimised, as shown in Fig. S2. The 1% Pt loading on SCN 550 exhibits the highest activity compared to 0.5% and 3% loading. The activity enhancement observed by 1% Pt loading might be due to the high concentration of Pt active sites available for the proton reduction reaction. Further increase of Pt to 3% shows a decreased performance, probably attributing to the "covering effect" [30], leading to obstruction of light absorption of photocatalyst and shielding the surface active sites. The reports on water-facilitated photocatalytic methanol conversion indicate that the water amount would play an important role [31,32]. Hence, the effect of water on methanol reforming on SCN 550 was investigated by changing the water ratio in the methanol mixture, and the results are shown in Fig. 2c. The H_2 generation activity in 100% methanol under full arc illumination is 0.8 mmol $g^{-1}h^{-1}$, which increases to 1.7 mmol $g^{-1}h^{-1}$ and 2.1 mmol $g^{-1}h^{-1}$ while increasing the water from 0% to 30% and 50%. This might be due to one more H_2 produced from water apart from H_2 from methanol. In the case of further increasing the water content to 70%, the H_2 evolution is reduced to 0.7 mmol $g^{-1}h^{-1}$. It might be due to less methanol involved in the reaction. Hence, optimisation of water content in methanol-reforming is crucial.

Several intermediates (eg. HCHO and HCOOH) were reported before during water reforming of methanol as methanol underwent step-by-

step oxidation to finally produce CO_2. The oxidation product selectivity using SCN 550 was studied by measuring the by-products. Interestingly, no HCHO and HCOOH liquid products were detected (Fig. S3 and S4). Moreover, only gaseous products including CO_2 and H_2 were obtained during the reaction (Fig. 2d). Impressively, the average ratio of H_2/CO_2 is almost 2.97, which is very close to the theoretical ratio of 3 in water reforming of methanol ($CH_3OH + H_2O \rightarrow CO_2 + 3H_2$) [33], suggesting the crucial role of water in the reaction for efficient H_2 evolution. To confirm the H origin, H isotope measurement was performed via MAT253 isotope ratio mass spectrometer [34]. All hydrogen isotope values are reported in the conventional per mil (‰) notation with reference to Vienna Standard Mean Ocean Water (VSMOW). The standard hydrogen gas (99.999%) was used as the reference gas, comprising H_2 and small portion of HD with the δ^2HVSMOW value (HD/H_2) of 20%. The reference gas was injected twice (reference gas 1 and 2) to ensure a reliable measurement. From Fig. S5 and Table S1, one can see the major product by water reforming of methanol on SCN 550 is HD. In other words, the per mil (‰) notations are 205.92 and 99502.05 for the reference H_2 and the gas (HD) produced by water reforming of methanol on SCN 550, respectively. Such a much higher value obtained from the sample gas indicates the HD originate from both methanol and water. In addition, it is found that H_2 can be produced under different visible light irradiation (Fig. S6).

Generally, increasing the temperature enhances the reaction kinetics of H_2 production. To test this hypothesis, the photocatalytic water reforming of methanol at different temperatures such as 25 °C, 70 °C and 90 °C were measured (Fig. S7). As anticipated, the rate of H_2 evolution increases while increasing the temperature from 25 °C to 70 °C and further enhancement is observed at 90 °C. In a control experiment, the H_2 evolution activity of SCN 550 under the dark condition at 90 °C was tested and no H_2 evolution was obtained, indicating the H_2 generation is from the photocatalytic reaction rather than thermal methanol decomposition. It was reported that the alkaline condition favours water reforming of methanol as the –OH groups in the solution facilitate the conversion of intermediates [4]. To study the role of OH, the H_2 evolution activity at various pH values ranging from 7 to 13 was measured under full-spectrum irradiation. It can be seen from Fig. S8 that the H_2 generation activity is increased when pH changes from 7 to 12, which is probably due to more OH radicals available at higher pH values that reacted with the formed intermediates such as HCOOH to produce H_2 and CO_2. The best activity is observed at pH 12 up to 5.4 mmol $g^{-1}h^{-1}$. Further pH increase to 13 leads to a remarkably reduced H_2 evolution, which might be because of the reduced number of protons in water available for H_2 production.

Based on the above experimental results, the H_2 evolution activity of SCN 550 at the optimal pH 12 while at different temperatures was evaluated. As expected, the best activity (14.7 mmol $g^{-1}h^{-1}$) is obtained at 90 °C (Fig. 2e). The AQE under the optimised condition reaches 29% at 365 nm, which is higher than the best sulphur doped carbon nitride reported before as listed in Table S2. In Table S2, the sulphur in these S doped g-C_3N_4 reported before was doped in the heptazine ring while the sulphur of SCN in this work was at terminal C-S-H and N-S-H sites. Moreover, the presence of carbon vacancies discussed below facilitated the charge separation, thus providing efficient H_2 evolution. Such a precursor derived C-S-H and N-S-H as the sulphur introduction sites are the major difference from the published.

The activation energy of SCN 550 was estimated to be 13.1 kJ mol^{-1}, derived from the Arrhenius plot. The enhanced activity might be due to the controlled sulphur doping position in g-C_3N_4 as discussed below, further promoting methanol adsorption, light-harvesting and charge separation. It is essential to test the stability of the photocatalyst under the present experimental conditions. Hence, the photocatalytic water reforming of methanol using SCN 550 was tested for a prolonged time (95 h), in which Ar re-purging was performed every 19 h. The activity is linearly increased during the photocatalytic reaction, and no obvious change is observed in each run (Fig. 2f), indicating the SCN 550 sample has excellent stability. The slight activity fluctuation might be due to the error caused by the manual gas injection. Moreover, the XRD spectra of the SCN 550 sample before and after 95 h reaction (Fig. S9) exhibits no noticeable differences, further confirming the long-term stability of SCN 550.

3.3. Mechanism investigation

The optical absorption of g-C_3N_4 and various SCN samples was studied by the UV Vis DRS spectroscopy as shown in Fig. 3a. The reference g-C_3N_4 exhibits a typical photo-absorption edge at 450 nm, ascribing to the intrinsic π-π* transitions [35]. The SCN 500 and SCN 550 show a noticeable red shift suggesting the narrower band gap, which is beneficial to harvesting visible-light photons. The increased absorption around 500 nm of all SCN photocatalysts is assigned to the n-π* excitation originating from the distorted structure [36]. Moreover, such distortion triggers the colour change of samples (the insert of Fig. 3a), which might be due to the linker alteration, allowing more electrons to involve in n-π* excitation [37]. Tauc plots were applied using the DRS data and obtained the band gaps of g-C_3N_4, SCN 500, SCN 550 and SCN 600, which are 2.7 eV, 2.5 eV, 2.6 eV and 2.7 eV (Fig. 3b), respectively.

To study the impact of S concentration in g-C_3N_4 on water reforming of methanol rates, all samples underwent elemental analysis. The reference g-C_3N_4 exhibits an average N/C ratio of 1.33 (Fig. 3c), very close to the standard stoichiometric ratio [38]. Comparatively, the N/C ratio is increased in all SCN samples, probably due to the carbon defect formed in SCN during the polymerisation. When the calcination temperature increases from 500 °C to 550 °C, the S concentration (Fig. S10) shows an apparent decrease from 2.10 % to 0.21 %, which is probably ascribed to the removal of S at a higher temperature. This result also matches with the FTIR spectra, where low S doping leads to the obvious enhanced -NHx groups. Furthermore, the S content is somewhat increased to 0.49 % while annealing at 600 °C, suggesting that both sulphur and carbon removal happens at a higher temperature. Considering the H_2 production rate obtained using the overall SCN samples, the S amount is not proportional to the observed H_2 generation activity as the sample prepared at 550 °C shows the highest activity. So the position of the doped S in g-C_3N_4 should be investigated.

To explore the structure of SCN, 13C solid NMR spectra of g-C_3N_4 and SCN samples were measured (Fig. S11), and the signal at 157 ppm in all samples corresponding to CN_3 moieties. The peak at 165 nm corresponds to $CN_2(NH_2)$ of g-C_3N_4, which slightly shifts to 164 ppm in S-incorporated g-C_3N_4 samples due to the more $CN_2(NH)$ formed [40]. Such a shift is also indicative of the linker effect, attributing to fewer NH_2 groups and the formation of S terminal groups in SCN, thus changing the chemical environment of carbon. The SCN samples show similar two main peaks to the reference g-C_3N_4, without the appearance of any new peaks, excluding that sulphur was doped in the CN-conjugated network.

The EPR was carried out to figure out the vacancy in g-C_3N_4 and SCN samples, as shown in Fig. 3d. It has been reported that the unpaired electrons are usually considered to derive from carbon vacancies [41,42]. The g-C_3N_4 has a small signal while all SCN photocatalysts show stronger signals, suggesting that the carbon atom loss after sulphur introduction causes more unpaired electrons. As the synthesis temperature increases, the EPR signal shows an increase, suggesting more carbon vacancies are produced at higher temperatures. This can explain the higher N/C ratio in samples SCN 600 prepared at a higher temperature than SCN 550.

To confirm the S doping position and chemical states of the elements in SCN, XPS was performed. The C1s spectra (Fig. 4a) consist of four separate peaks at 284.8 eV, 286.3 eV and 288.0 eV, assigning to the C–C bond, C-N or C-S bond, sp^2-bonded carbon (N-C = N), respectively [43]. The signal of C-S or C-N indicates a decrease when the calcination temperature increases from 500 °C to 550 °C and further decreases at 600 °C, suggesting that fewer C-S or C-N, this result is in part consistent

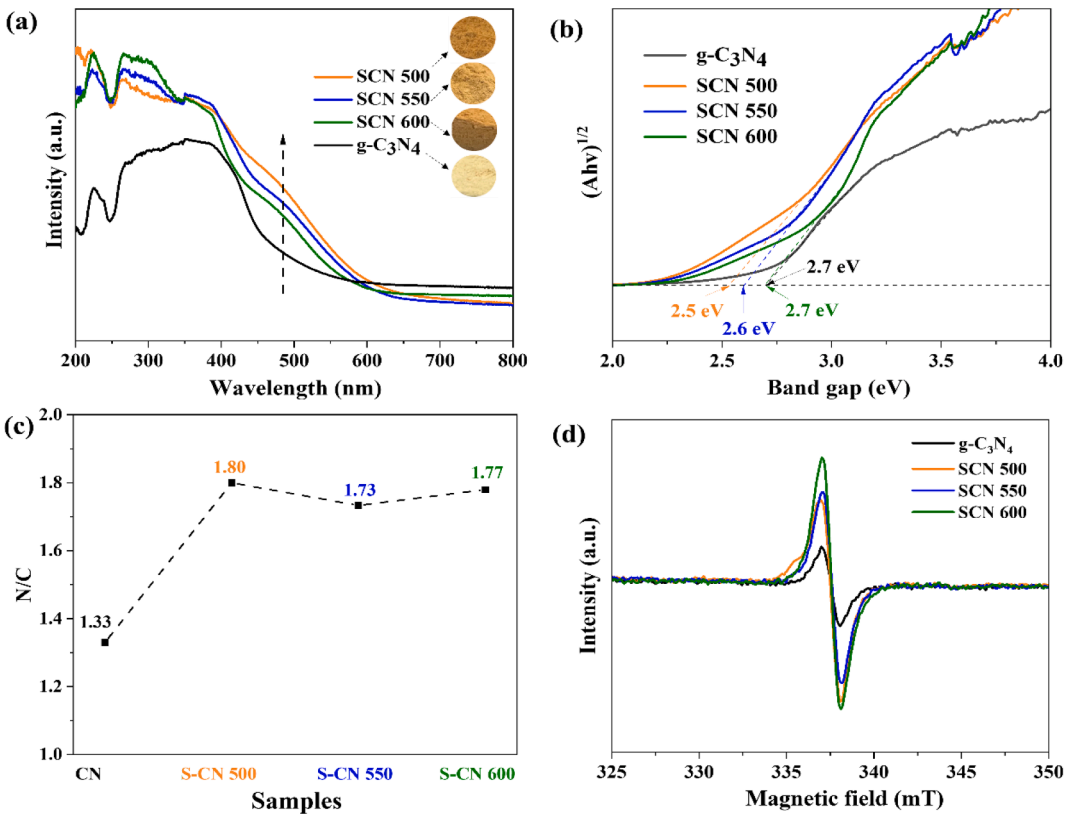

Fig. 3. (a) UV–Vis DRS spectra, (b) Tauc plots were plotted using the DRS data, (c) the ratio of N/C determined from Element Analysis (d) EPR spectra of g-C_3N_4 and SCN samples.

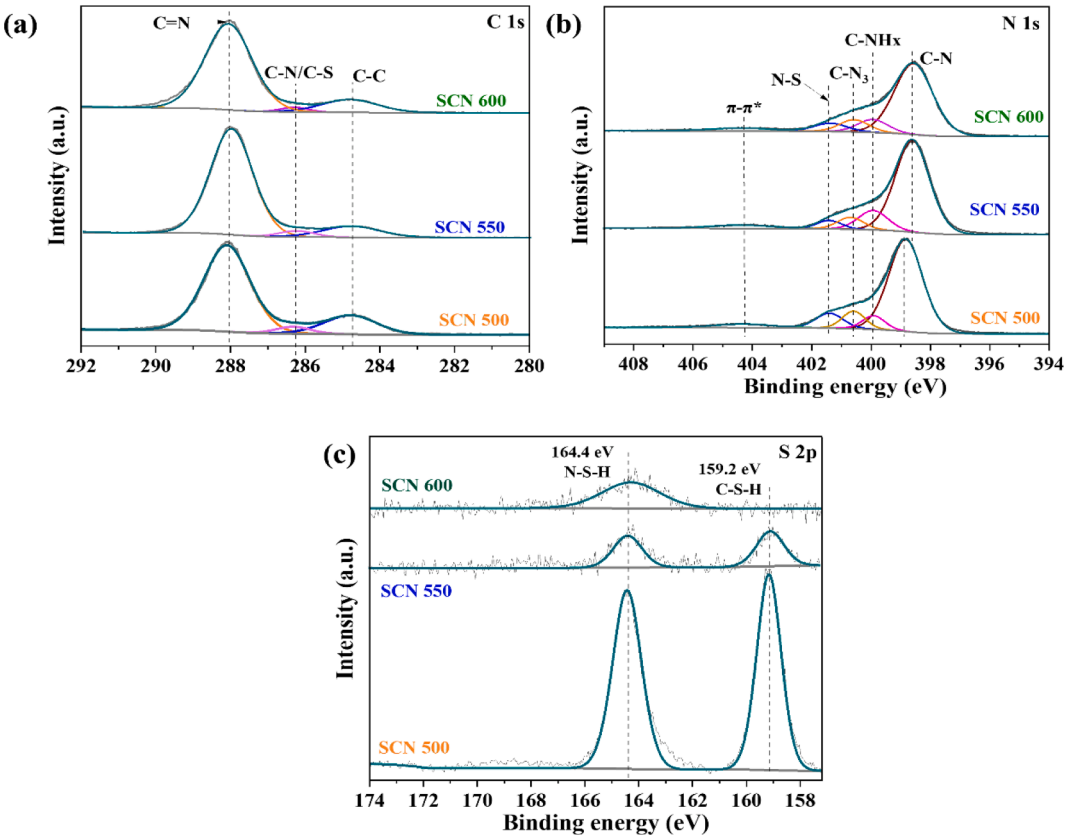

Fig. 4. The XPS spectra of SCN550 (a) C 1 s, (b) N 1 s, (c) S 2p.

with the EPR. The N 1 s spectra (Fig. 4b) are deconvoluted into heptazine C-N at 398.5–398.8 eV, C-NHx at 400.0 eV, N-$(C)_3$ at 400.6 eV, C-N–H at 401.4 eV and π-π* at 404.3 eV [22]. Those characteristic peaks suggest the structure of the typical g-C_3N_4 skeleton present in SCN samples. To reveal the oxidation states of S, the S 2p XPS spectra of various SCN samples were measured and compared in Fig. 4c, showing noticeable peak differences in each photocatalyst. The peak at 159.2 eV is attributed to C-S-H [44], while the peak at 164.4 eV is assigned to the N-S-H [20,45,46]. The SCN 500 exhibits a more apparent S 2p spectrum than SCN 550 and SCN 600, suggesting the presence of high sulphur content in SCN 500, which is in good agreement with the elemental analysis data shown in Fig. S10. These results show that the S has been incorporated in all SCN samples. Interestingly, the binding energy of C-S-H is smaller than some reported (160–161 eV) [47], indicating the enhanced electron density in SCN samples. Comparatively, the SCN 600 sample only shows N-S-H without a C-S-H footprint as the high temperature enables S in the terminal C-S-H or N-S-H bonds to be decomposed easily, leading to the absence of terminal -S-H in SCN 600. This phenomenon is consistent with the C-S intensity reduction in C 1 s of SCN 600. Taking into account the activity order of SCN 550 > SCN 600 > SCN 500, and the order of C-S-H (Table S3) ratio in three samples is (SCN 550 (51.2%) > SCN 500 (48.2%) > SCN 600 (0%), one can see that the C-S-H dominates activity rather than N-S-H while carbon vacancies might play some role as well for charge separation as indicated by PL later, which somehow promotes SCN 600 activity better than SCN 500. The N_2 adsorption study was performed and the result is shown in Fig. S12. The SCN 550 shows the BET surface area of 19.14 m^2/g, which is higher than the reference g-C_3N_4 (12.95 m^2/g). The increased BET surface area of the SCN sample is probably due to the porous structure, which also in part contributes to the enhanced catalytic activity [39].

The S introduction likely affects the band position, which was confirmed by measuring the XPS VB spectra as shown in Fig. S13. The VB of reference g-C_3N_4, SCN 500, SCN 550, and SCN 600 are determined to be 1.84 eV, 2.0 eV, 1.95 eV and 1.8 eV, respectively. To obtain a clear picture of band positions, the CB potential of the samples was determined by Mott-Schottky plot flat-band potential (E_{fb}) measurement as shown in Fig. 5a. The SCN 550 exhibits a less negative E_{fb} (-0.65 vs. RHE) than g-C_3N_4 (-0.86 vs. RHE), which is consistent with the calculated CB from the measured band gap value and the XPS VB potential. Although the CB band position of SCN 550 shows a slightly positive shift compared with g-C_3N_4, it still has a negative enough potential for the proton reduction reaction. The more positive VB of SCN 550 should be beneficial to drive the methanol oxidation to CO_2. The band structure of g-C_3N_4 and SCN 550 is displayed in Fig. 5b, suggesting that the sulphur introduction induces the narrowed bandgap and positive shift of band positions.

In addition, the charge separation and transfer kinetics of g-C_3N_4 and SCN 550 were investigated by EIS. From the EIS Nyquist plots in Fig. 5c, SCN 550 electrode exhibits a smaller arc radius than g-C_3N_4, suggesting a lower charge transfer resistance of SCN 550, or a higher charge transfer rate than g-C_3N_4. Further, the corresponding fitting results of resistances and capacitances are depicted in Table S4. The equivalent circuit involved in the system can be represented as shown in the inset of Fig. 5c, where Rs is the resistance of the overall system, R_{Bulk} and CPE_1 are the resistance and capacitance at the FTO and photocatalyst interface, and Rct and CPE_2 are the charge transfer resistance and capacitance at the electrode–electrolyte interface. The Rct and R_{Bulk} of SCN 550 are measured to be 4.159×10^2 and 3.207×10^4 Ω cm^2, respectively, which are smaller than bare g-C_3N_4 (5.635×10^2 and 5.376×10^4). The reduced Rct should be attributed to the S- introduction, which is beneficial for enhanced charge transfer. These results emphasize that SCN can facilitate charge separation and transfer.

Photoluminescence (PL) spectroscopy was performed to explore charge carriers' recombination under 325 nm excitation. The peak

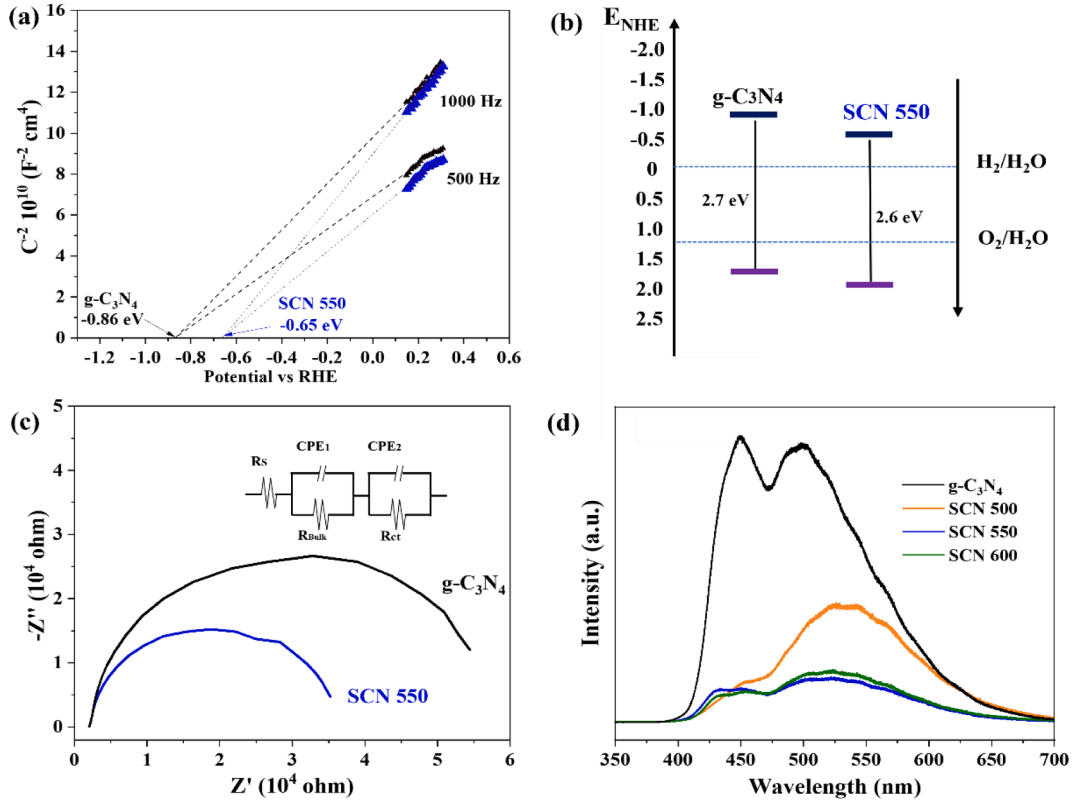

Fig. 5. (a) Mott-schottky plots and (b) Band structure of g-C_3N_4 and the optimal SCN 550, determined by Mott-schottky plots, XPS valence-band and UV–Vis spectra. (c) The electrochemical impedance spectra (EIS) of g-C_3N_4 and SCN 550. The corresponding EIS circuit is shown in the insert. (d) Photoluminescence spectra of g-C_3N_4 and SCN samples using 325 nm as the excitation wavelength.

intensity reveals the radiative recombination rate of photoexcited electrons and holes. Fig. 5d shows the PL spectra of g-C_3N_4 and SCN samples. All samples exhibit two peaks, one at 450 nm and the other at 520 nm, attributing to $\pi - \pi^*$ transitions and $n - \pi^*$ emission, respectively [22]. Moreover, the SCN photocatalysts show significantly decreased intensity compared with g-C_3N_4, suggesting the charge recombination is suppressed in SCN samples [48]. This might be due to efficient charge separation induced by the S dopant. In detail, SCN 500 exhibits a visibly higher PL signal than SCN 550 and SCN 600, probably due to too much sulphur introduction. While the decreased PL intensity in SCN 550 and SCN 600 can be attributed to more carbon vacancies which might reduce the recombination of photoexcited charges, as indicated by the EPR result.

Based on the above characterisations, the following is proposed for enhanced activity by SCN. On one hand, the S-doping sites lead to the narrow bandgap that enables SCN to absorb a bit more visible photons, thereby increasing the generation of more photoexcited charge carriers. On the other hand, C-S-H formation plays a critical role in facilitating charge separation and transfer. Hence, enhanced light absorption and faster charge separation are two main reasons responsible for the higher activity of SCN than pure g-C_3N_4.

4. Conclusion

In summary, a green route for water reforming of methanol into H_2 and CO_2 has been successfully proved using SCN as the photocatalysts that were prepared using a self-assembly strategy. The H_2 generation activity of SCN was 7 times higher than that of the reference g-C_3N_4 under visible light irradiation. The optimized SCN photocatalyst (prepared at 550 ℃) successfully produced H_2 with a rate of 14.7 mmol $g^{-1}h^{-1}$ and exhibited long-term stability up to 95 h, together with an AQE of nearly 30% and the activation energy of 13.1 kJ mol^{-1}. More importantly, it produced only gaseous H_2 and CO_2 with the ideal stoichiometry of 3:1, strongly indicating the water reforming of methanol process. The introduction of sulphur into g-C_3N_4 has successfully narrowed down the bandgap of the g-C_3N_4, which is beneficial to harvest more visible photons efficiently and enhance H_2 production. Furthermore, the PL and EIS experimental results suggested that the better charge separation was achieved after S-doping, which is mainly due to the terminal C-S-H sites.

Declaration of Competing Interest

The authors declare that they have no known competing financial interests or personal relationships that could have appeared to influence the work reported in this paper.

Acknowledgements

All authors thank UK EPSRC (EP/S018204/2), Leverhulme Trust (RPG-2017-122), Royal Society Newton Advanced Fellowship grant (NAF\R1\191163), Royal Society International Exchange Scheme (IEC \NSFC\170342) and Royal Society Leverhulme Trust Senior Research Fellowship (SRF\R1\21000153).

Appendix A. Supplementary data

Supplementary data to this article can be found online at https://doi.org/10.1016/j.cej.2022.136790.

References

[1] R.D. Cortright, R.R. Davda, J.A. Dumesic, Hydrogen from catalytic reforming of biomass-derived hydrocarbons in liquid water, Nature 418 (2002) 289–292, https://doi.org/10.1142/9789814317665_0043.
[2] K.I. Fujita, R. Kawahara, T. Aikawa, R. Yamaguchi, Hydrogen production from a methanol-water solution catalyzed by an anionic iridium complex bearing a functional bipyridonate ligand under weakly basic conditions, Angew. Chemie - Int. Ed. 54 (2015) 9057–9060, https://doi.org/10.1002/anie.201502194.
[3] D. Kong, X. Han, J. Xie, Q. Ruan, C.D. Windle, S. Gadipelli, K. Shen, Z. Bai, Z. Guo, J. Tang, Tunable covalent triazine-based frameworks (CTF-0) for visible-light-driven hydrogen and oxygen generation from water splitting, ACS Catal. 9 (2019) 7697–7707, https://doi.org/10.1021/acscatal.9b02195.
[4] M. Nielsen, E. Alberico, W. Baumann, H.J. Drexler, H. Junge, S. Gladiali, M. Beller, Low-temperature aqueous-phase methanol dehydrogenation to hydrogen and carbon dioxide, Nature 495 (2013) 85–89, https://doi.org/10.1038/nature11891.
[5] A. Kudo, Y. Miseki, Heterogeneous photocatalyst materials for water splitting, Chem. Soc. Rev. 38 (2009) 253–278, https://doi.org/10.1039/b800489g.
[6] D.J. Martin, K. Qiu, S.A. Shevlin, A.D. Handoko, X. Chen, Z. Guo, J. Tang, Highly efficient photocatalytic H2 evolution from water using visible light and structure-controlled graphitic carbon nitride, Angew. Chemie - Int. Ed. 53 (2014) 9240–9245, https://doi.org/10.1002/anie.201403375.
[7] K. Maeda, X. Wang, Y. Nishihara, D. Lu, M. Antonietti, K. Domen, Photocatalytic activities of graphitic carbon nitride powder for water reduction and oxidation under visible light, J. Phys. Chem. C. 113 (12) (2009) 4940–4947.
[8] V.-H. Lau, M.B. Mesch, V. Duppel, V. Blum, J. Senker, B.V. Lotsch, Low-molecular-weight carbon nitrides for solar hydrogen evolution, J. Am. Chem. Soc. 137 (3) (2015) 1064–1072.
[9] X. Wang, K. Maeda, A. Thomas, K. Takanabe, G. Xin, J.M. Carlsson, K. Domen, M. Antonietti, A metal-free polymeric photocatalyst for hydrogen production from water under visible light, Nat. Mater. 8 (2009) 76–80, https://doi.org/10.1038/nmat2317.
[10] A. Thomas, A. Fischer, F. Goettmann, M. Antonietti, J.O. Müller, R. Schlögl, J. M. Carlsson, Graphitic carbon nitride materials: Variation of structure and morphology and their use as metal-free catalysts, J. Mater. Chem. 18 (2008) 4893–4908, https://doi.org/10.1039/b800274f.
[11] M. Liu, M. Gao, L. Pei, Y. Ji, X. Gu, H. Wang, H. Tan, J. Zhao, J. Jia, Z. Zheng, Tailoring phenol photomineralization pathway over polymeric carbon nitride with cyano group multifunctional active sites, Appl. Catal. B Environ. 284 (2021), 119710, https://doi.org/10.1016/j.apcatb.2020.119710.
[12] S. Chen, Z. Yang, J. Chen, J. Liao, S. Yang, F. Peng, L.X. Ding, G. Yang, S. Zhang, Y. Fang, Electron-rich interface of Cu-Co heterostructure nanoparticle as a cocatalyst for enhancing photocatalytic hydrogen evolution, Chem. Eng. J. 434 (2022), 134673, https://doi.org/10.1016/j.cej.2022.134673.
[13] S. Chen, J. Liao, Z. Zhou, S. Yang, Q. Gao, X. Cai, F. Peng, Y. Fang, S. Zhang, Boosting photocatalytic hydrogen evolution using a noble-metal-free co-catalyst: CuNi@C with oxygen-containing functional groups, Appl. Catal. B Environ. 291 (2021), 120139, https://doi.org/10.1016/j.apcatb.2021.120139.
[14] S. Chen, Y. Hau Ng, J. Liao, Q. Gao, S. Yang, F. Peng, X. Zhong, Y. Fang, S. Zhang, FeCo alloy@N-doped graphitized carbon as an efficient cocatalyst for enhanced photocatalytic H2 evolution by inducing accelerated charge transfer, J. Energy Chem. 52 (2020) 92–101, https://doi.org/10.1016/j.jechem.2020.04.040.
[15] L. Jiang, X. Yuan, Y. Pan, J. Liang, G. Zeng, Z. Wu, H. Wang, Doping of graphitic carbon nitride for photocatalysis: A reveiw, Appl. Catal. B Environ. 217 (2017) 388–406, https://doi.org/10.1016/j.apcatb.2017.06.003.
[16] H. Li, J. Shang, J. Shi, K. Zhao, L. Zhang, Facet-dependent solar ammonia synthesis of BiOCl nanosheets via a proton-assisted electron transfer pathway, Nanoscale. 8 (2016) 1986–1993, https://doi.org/10.1039/c5nr07380d.
[17] S. Guo, Z. Deng, M. Li, B. Jiang, C. Tian, Q. Pan, H. Fu, Phosphorus-doped carbon nitride tubes with a layered micro- nanostructure for enhanced visible-light photocatalytic hydrogen evolution, Angew Chem Int Ed. 128 (5) (2016) 1862–1866.
[18] J. Zhang, X. Chen, K. Takanabe, K. Maeda, K. Domen, J.D. Epping, X. Fu, M. Antonietti, X. Wang, Synthesis of a carbon nitride structure for visible-light catalysis by copolymerization, Angew Chem Int Ed. 49 (2010) 441–444, https://doi.org/10.1002/anie.200903886.
[19] J. Zhang, J. Sun, K. Maeda, K. Domen, P. Liu, M. Antonietti, X. Fu, X. Wang, Sulfur-mediated synthesis of carbon nitride: Band-gap engineering and improved functions for photocatalysis, Energy Environ. Sci. 4 (2011) 675–678, https://doi.org/10.1039/c0ee00418a.
[20] G. Liu, P. Niu, C. Sun, S.C. Smith, Z. Chen, G.Q. Lu, H.M. Cheng, Unique electronic structure induced high photoreactivity of sulfur-doped graphitic C_3N_4, J. Am. Chem. Soc. 132 (2010) 11642–11648, https://doi.org/10.1021/ja103798k.
[21] W.-J. Ong, L.-L. Tan, Y.H. Ng, S.-T. Yong, S.-P. Chai, Graphitic carbon nitride (g-C 3 N 4)-based photocatalysts for artificial photosynthesis and environmental remediation: are we a step closer to achieving sustainability? Chem. Rev. 116 (12) (2016) 7159–7329.
[22] Y. Wang, M.K. Bayazit, S.J.A. Moniz, Q. Ruan, C.C. Lau, N. Martsinovich, J. Tang, Linker-controlled polymeric photocatalyst for highly efficient hydrogen evolution from water, Energy Environ. Sci. 10 (2017) 1643–1651, https://doi.org/10.1039/c7ee01109a.
[23] T. Hisatomi, K. Takanabe, K. Domen, Photocatalytic water-splitting reaction from catalytic and kinetic perspectives, Catal. Letters. 145 (2015) 95–108, https://doi.org/10.1007/s10562-014-1397-z.
[24] B. Kumru, D. Cruz, T. Heil, M. Antonietti, In situ formation of arrays of tungsten single atoms within carbon nitride frameworks fabricated by one-step synthesis through monomer complexation, Chem. Mater. 32 (2020) 9435–9443, https://doi.org/10.1021/acs.chemmater.0c03616.
[25] J. Zhang, M. Zhang, C. Yang, X. Wang, Nanospherical carbon nitride frameworks with sharp edges accelerating charge collection and separation at a soft photocatalytic interface, Adv. Mater. 26 (2014) 4121–4126, https://doi.org/10.1002/adma.201400573.

[26] W. Jiang, Q. Ruan, J. Xie, X. Chen, Y. Zhu, J. Tang, Oxygen-doped carbon nitride aerogel : A self-supported photocatalyst for solar-to-chemical energy conversion, Appl. Catal. B Environ. 236 (2018) 428–435, https://doi.org/10.1016/j.apcatb.2018.05.050.
[27] L. Lin, W. Ren, C. Wang, A.M. Asiri, J. Zhang, X. Wang, Crystalline carbon nitride semiconductors prepared at di ff erent temperatures for photocatalytic hydrogen production, Appl. Catal. B Environ. 231 (2018) 234–241, https://doi.org/10.1016/j.apcatb.2018.03.009.
[28] Y. Qu, X. Duan, Progress, challenge and perspective of heterogeneous photocatalysts, Chem. Soc. Rev. 42 (2013) 2568–2580, https://doi.org/10.1039/c2cs35355e.
[29] M.o. Zhang, W. Jiang, D.i. Liu, J. Wang, Y. Liu, Y. Zhu, Y. Zhu, Photodegradation of phenol via C3N4-agar hybrid hydrogel 3D photocatalysts with free separation, Appl. Catal B, Environ. 183 (2016) 263–268.
[30] X. Li, Y. Pi, L. Wu, Q. Xia, J. Wu, Z. Li, J. Xiao, Facilitation of the visible light-induced Fenton-like excitation of H2O2 via heterojunction of g-C3N4/NH2-Iron terephthalate metal-organic framework for MB degradation, Appl. Catal. B Environ. 202 (2017) 653–663, https://doi.org/10.1016/j.apcatb.2016.09.073.
[31] W. Yang, Z. Geng, Q. Guo, D. Dai, X. Yang, Effect of multilayer methanol and water in methanol photochemistry on TiO2, J. Phys. Chem. C. 121 (2017) 17244–17250, https://doi.org/10.1021/acs.jpcc.7b04224.
[32] B.B. Xu, M. Zhou, R. Zhang, M. Ye, L.Y. Yang, R. Huang, H.F. Wang, X.L. Wang, Y. F. Yao, Solvent water controls photocatalytic methanol reforming, J. Phys. Chem. Lett. 11 (2020) 3738–3744, https://doi.org/10.1021/acs.jpclett.0c00972.
[33] D.R. Palo, R.A. Dagle, J.D. Holladay, Methanol steam reforming for hydrogen production, Chem. Rev. 107 (2007) 3992–4021, https://doi.org/10.1021/cr050198b.
[34] M.E. Popa, D. Paul, C. Janssen, T. Röckmann, H_2 clumped isotope measurements at natural isotopic abundances, Rapid Commun. Mass Spectrom. 33 (2019) 239–251, https://doi.org/10.1002/rcm.8323.
[35] K. Saravanakumar, C.M. Park, Rational design of a novel $LaFeO_3$/g-C_3N_4/$BiFeO_3$ double Z-scheme structure: Photocatalytic performance for antibiotic degradation and mechanistic insight, Chem. Eng. J. 423 (2021), 130076, https://doi.org/10.1016/j.cej.2021.130076.
[36] Y. Chen, B. Wang, S. Lin, Y. Zhang, X. Wang, Activation of n- π^* transitions in two-dimensional conjugated polymers for visible light photocatalysis, J. Phys. Chem. C. 118 (2014) 29981–29989, https://doi.org/10.1021/jp510187c.
[37] A.B. Jorge, D.J. Martin, M.T.S. Dhanoa, A.S. Rahman, N. Makwana, J. Tang, A. Sella, F. Corà, S. Firth, J.A. Darr, P.F. McMillan, H_2 and O_2 evolution from water half-splitting reactions by graphitic carbon nitride materials, J. Phys. Chem. C. 117 (2013) 7178–7185, https://doi.org/10.1021/jp4009338.
[38] V.N. Khabashesku, J.L. Zimmerman, J.L. Margrave, Powder synthesis and characterization of amorphous carbon nitride, Chem. Mater. 12 (2000) 3264–3270, https://doi.org/10.1021/cm000328r.
[39] F. Su, C.K. Poh, J.S. Chen, G. Xu, D. Wang, Q. Li, J. Lin, X.W. Lou, Nitrogen-containing microporous carbon nanospheres with improved capacitive properties, Energy Environ. Sci. 4 (2011) 717–724, https://doi.org/10.1039/c0ee00277a.
[40] B.V. Lotsch, M. Döblinger, J. Sehnert, L. Seyfarth, J. Senker, O. Oeckler, W. Schnick, Unmasking melon by a complementary approach employing electron diffraction, solid-state NMR spectroscopy, and theoretical calculations - Structural characterization of a carbon nitride polymer, Chem. - A Eur. J. 13 (2007) 4969–4980, https://doi.org/10.1002/chem.200601759.
[41] G. Fanchini, S.C. Ray, A. Tagliaferro, E. Laurenti, Paramagnetic centres and microstructure of reactively sputtered amorphous carbon nitride thin films, Diam. Relat. Mater. 11 (2002) 1143–1148, https://doi.org/10.1016/S0925-9635(01)00715-4.
[42] M. Tabbal, T. Christidis, S. Isber, P. Mérel, M.A. El Khakani, M. Chaker, A. Amassian, L. Martinu, Correlation between the sp 2-phase nanostructure and the physical properties of unhydrogenated carbon nitride, J. Appl. Phys. 98 (4) (2005) 044310.
[43] H. Wang, Y. Bian, J. Hu, L. Dai, Highly crystalline sulfur-doped carbon nitride as photocatalyst for efficient visible-light hydrogen generation, Appl. Catal. B Environ. 238 (2018) 592–598, https://doi.org/10.1016/j.apcatb.2018.07.023.
[44] S.F. Ng, M.Y.L. Lau, W.J. Ong, Lithium–sulfur battery cathode design: tailoring metal-based nanostructures for robust polysulfide adsorption and catalytic conversion, Adv. Mater. 33 (2021) 1–54, https://doi.org/10.1002/adma.202008654.
[45] G. Zhao, A. Wang, W. He, Y. Xing, X. Xu, 2D new nonmetal photocatalyst of sulfur-doped h-BN nanosheeets with high photocatalytic activity, Adv. Mater. Interfaces. 6 (2019) 1–7, https://doi.org/10.1002/admi.201900062.
[46] Y. Chen, F. Su, H. Xie, R. Wang, C. Ding, J. Huang, Y. Xu, L. Ye, One-step construction of S-scheme heterojunctions of N-doped MoS_2 and S-doped g-C_3N_4 for enhanced photocatalytic hydrogen evolution, Chem. Eng. J. 404 (2021), 126498, https://doi.org/10.1016/j.cej.2020.126498.
[47] K. Wang, Q. Li, B. Liu, B. Cheng, W. Ho, J. Yu, Applied Catalysis B : Environmental Sulfur-doped g-C_3N_4 with enhanced photocatalytic CO_2 -reduction performance, Appl. Catal. B, Environ. 176–177 (2015) 44–52, https://doi.org/10.1016/j.apcatb.2015.03.045.
[48] L.G. Devi, R. Kavitha, A review on non metal ion doped titania for the photocatalytic degradation of organic pollutants under UV/solar light: Role of photogenerated charge carrier dynamics in enhancing the activity, Appl. Catal. B Environ. 140–141 (2013) 559–587, https://doi.org/10.1016/j.apcatb.2013.04.035.